Carbonic anhydrase IX-targeted chemodynamic & photodynamic cancer stem cell therapy

Hyo Sung Jung
Hyupsung University
Seyoung Koo
Korea University
Miae Won
Korea University
Seeun An
Hyupsung University https://orcid.org/0000-0002-5360-2334
Haebeen Park
Hyupsung University
Jonathan Sessler
The University of Texas at Austin https://orcid.org/0000-0002-9576-1325
Jiyou Han
Korea University
Jong Seung Kim (jongskim@korea.ac.kr)
Korea University https://orcid.org/0000-0003-3477-1172

Article

Keywords:

Posted Date: May 20th, 2022

DOI: https://doi.org/10.21203/rs.3.rs-1677001/v1

Abstract

Chemoresistance originating from cancer stem cells (CSCs) is a major cause of cancer treatment failure and highlights the need to develop CSC-targeting therapies. Although enormous progress in both photodynamic therapy (PDT) and chemodynamic therapy (CDT) has been made in recent decades, the efficacy of these modalities against CSC remains limited. Here, we report a new generation photosensitizer, CA9-BPS-Cu(II), a system that combines three subunits within a single molecule, namely a copper catalyst for CDT, a boron dipyrromethene photosensitizer for PDT, and acetazolamide for CSC targeting via carbonic anhydrase-9 (CA9) binding. A therapeutic effect in MDA-MB-231 cells was observed that is ascribed to elevated oxidative stress mediated by a combined CDT/PDT effect, as well as through copper-catalyzed glutathione oxidation. The CSC targeting ability of CA9-BPS-Cu(II) was evident from its specific affinity for CD133-positive MDA-MB-231 cells. Moreover, its efficacy was successfully demonstrated in a xenograft mouse tumor model.

Introduction

Cancer stem cells (CSCs) represent a small, highly tumorigenic subset of cancer cells recognized for their self-renewal capacity, multipotent differentiation, and propensity for sphere formation[1]. CSCs have been found in most solid tumor types, including triple-negative breast cancer, and are linked to tumor recurrence and relapse following initial cancer treatment[2]. Unfortunately, the current therapeutic approaches, including photodynamic therapy (PDT) and chemodynamic therapy (CDT), have little effect on CSCs. Advanced therapeutic strategies that could target and eradicate CSCs could improve the clinical outcomes by potentially reducing the risk of relapse after cancer treatment.

PDT is in clinical use for the treatment of skin cancer and several classes of subcutaneous tumors[3]. The scope of PDT continues to expand and a broad range of deep tissue solid tumors, including breast cancers, are now being targeted through interstitial and intra-operative approaches[4,5]. PDT typically relies on a combination of photo-irradiation and an appropriately chosen photosensitizer (PS) to produce singlet oxygen ($^1O_2$), a reactive oxygen species (ROS) that mediate cancer-killing effects, such as cell apoptosis, vascular degradation, and immune response[6,7]. Ideally, the underlying photoactivation occurs with minimal side effects and high selectivity, thus endowing PDT with favorable safety profiles compared to conventional cancer therapies. In light of this, PDT has been considered a promising therapeutic option for tumors and a complement for other conventional therapies; however, the development of severe hypoxia within tumors significantly reduces the PDT outcome. PDT-induced hypoxia arises because of oxygen depletion directly through the photosensitization process or indirectly by vasculature damage and typically triggers the hypoxia inducible factor (HIF)-mediated signaling cascade[8]. The resulting hypoxia and HIF signaling are considered potential contributors to CSC phenotypes[9], providing resistance to PDT[10]. To date, enormous progress has been devoted to improving PDT, including selecting efficient PSs[11], effecting delivery to appropriate biological loci[12], regulating the reaction environments (e.g., increasing effective O_2 levels[13] or decreasing cellular antioxidant levels[14]),

and combining it judiciously with other modalities[15]. However, there remains a need for more effective PDT methods and, in particular, developing CSC-targeted therapies remains a recognized therapeutic challenge[16].

CDT is well-known for its unique ROS production pattern that is independent of local oxygen concentrations. In many cases, it relies on intracellular chemical reactions to decrease tumor vasculature or mediate an immune response[17]. One key CDT reaction involves the conversion of hydrogen peroxide (H_2O_2) into the hydroxyl radical (·OH), which is a highly cytotoxic ROS capable of destroying cancer cells. Due to their abnormal metabolism, solid tumors are often characterized by high levels of H_2O_2 (100 μM–1 mM), rendering this approach viable[18,19]. Cu(I) ions are particularly effective redox-active catalysts that can trigger the formation of ·OH from H_2O_2 *via* Cu(I)-catalyzed Fenton-like reactions, including potentially in the acidic tumor microenvironment characteristic of many solid tumors. Cu(I) complexes are thus attractive for use in CDT[20-22]. However, the presence of free Cu(I) ions can trigger adverse toxicity effects[23,24]. Moreover, the cellular antioxidant system can limit the efficiency of CDT[25].

Thus, it is important to target active Cu(I) ions in cancer cells and, if possible, harness endogenous reductants to promote conversion of H_2O_2 into ·OH. Several endogenous reductants, including non-enzymatic reductants (glutathione (GSH), cysteine (Cys), ascorbic acid (AA), etc.), and enzymatic reductants (GSH-S-transferase (GST), GSH-reductase (GR), catalase (CAT), superoxide dismutase (SOD), thioredoxin (Trx), etc.) are considered to be expressed at high levels in most cancer cells[26]. Of these, GSH, whose concentration in cancer cells is considerably higher than in normal cells (0.5~10 mM *vs.* 2–20 μM), is arguably the best established biological antioxidant[27].

Therefore, we sought to design a Cu(II) ion-containing PS that would be stable in cellular environments and release a Cu(I) ion upon interaction with GSH and potentially other endogenous reductants, such as Cys and AA. This free Cu(I), in turn, would be expected to react with local H_2O_2 to produce toxic ·OH *via* a chemodynamic process. Since the concentrations of endogenous reductants and H_2O_2 are expected to be higher in cancer cells, this approach might allow for a tumor-specific effect while also providing good cancer-killing efficiency.

The use of PDT, in combination with other treatment modalities, such as CDT, represents an attractive approach to improving therapeutic outcomes[28]. To date, the combined effect of CDT and PDT has been shown to provide superior therapeutic effects in model studies, an observation that is rationalized in terms of the PDT-induced ROS acting as a substrate for CDT, thereby providing a synergistic effect[29,30]. Several agents (*e.g.*, manganese silicate/calcium peroxide/indocyanine green nanoagents[31], copper ferrite nanoagents[32], porphyrin-ferrocene conjugates[33], ROS-activatable liposomes[34], copper/manganese silicate nanospheres[35], etc.) that rely on different strategies, including GSH-depletion, hypoxia relief, and H_2O_2 supplementation, have been studied for improving therapeutic efficacy; however, to the best of our knowledge, the use of such strategies to target and eradicate CSCs has yet to be reported.

We thus felt that combining a PDT PS and Cu(I)-based CDT could be further enhanced by CSC targeting. Recent work has shown that targeting carbonic anhydrase IX (CA9) using an acetazolamide moiety can be useful in this regard[36,37]. CA9 is a tumor-associated enzyme present at low levels in normal cells, but which is overexpressed in solid cancer cells[38-40]. CA9 is also emerging as a significant therapeutic target to deplete CSCs selectively because it is a driver of 'stemness' including Notch1 and Jagged1 of CSCs and the expression of epithelial-mesenchymal transition (EMT) markers and regulators[41]. Recently, Lock *et al.* reported that inhibition of CA9 with CA9-specific inhibitors led to significant depletion of CSCs within orthotopic breast tumor models[41]. In particular, an enhanced therapeutic effect was observed *in vivo* in metastatic lung cancer mouse models after CA9 knockdown and treatment with the anticancer drug, paclitaxel.

In this study we report a CA9-targeting copper-PS complex, **CA9-BPS-Cu(II)**, specifically designed to combine chemo- and photodynamic effects with an acetazolamide-based approach to CSC targeting (Fig. 1). Based on a combination of *in vitro* and *in vivo* studies, we found that the **CA9-BPS-Cu(II)** system is effective at depleting CSCs in high CA9 breast cancer cells and retarding tumor growth under conditions of combined PDT and CDT. To the best of our knowledge, this is the first time these three disparate modalities (*i.e.*, CDT, PDT, and CSC targeting therapy) have been used as a single system involving synergistic effect to effectively target and eradicate CSCs.

Results And Discussion

Design and characterization of CA9-BPS and CA9-BPS-Cu(II). To design a putative anti-CSC sensitizer, an acetazolamide ligand was conjugated to a boron dipyrromethene (BODIPY) PS *via* a 2-picolyl-triazole copper-binding unit. BODIPY was chosen as the PS because of its good photo- and chemo-stability, high molar absorptivity, negligible photobleaching, and excellent bio-compatibility[42]. The 2-picolyl-triazole linker was expected to coordinate Cu(II) ions and release them as Cu(I) for CDT catalysis following endogenous reductant-mediated reduction and subsequent demetalation[43]. With such considerations in mind, the metal-free form of the CA9-targeting BODIPY PS used in this study (**CA9-BPS**) was synthesized as shown in Supplementary Fig. 1. The analytical results (ESI-MS data, ^{1}H NMR and ^{13}C NMR spectra) for **CA9-BPS** and other new compounds were fully consistent with the proposed structures (cf. Supplementary Figs. 27–48).

Initial support for the expectation that **CA9-BPS** would support Cu(II) complexation came from spectroscopic analyses. Addition of 1.0 equiv. of Cu(II) (as the perchlorate salt) to **CA9-BPS** (both in ethanol solution) led to a 9 nm red shift in the absorption feature at 654 nm. The emission band of **CA9-BPS** at 680 nm was also substantially quenched, presumably due to a MLCT-based heavy-metal ion effect (Figs. 2a and Supplementary Fig. 2)[44]. The changes in the fluorescence intensity as a function of added Cu(II) concentration could fit well to a 1:1 ligand: metal binding profile; however, poor fits were observed for a possible 2:1 complexation mode. Using a standard treatment as codified by Thordarson[45], the corresponding 1:1 binding constant was calculated to be $(1.61 \pm 0.07) \times 10^{5}$ M^{-1} in ethanol. The

MALDI-TOF/TOF-MS spectrum (Supplementary Fig. 3) and Job's plot analysis (Fig. 2c) of **CA9-BPS** treated with Cu(II) is also consistent with a 1:1 binding stoichiometry. Importantly, the Cu(II) complex of **CA9-BPS** was found to be stable in PBS buffered solution (pH 7.4, 10 mM) containing 5% DMSO (Figs. 2b and 2d-f). However, the addition of 30 μM of GSH led to a significant recovery in the fluorescence intensity of **CA9-BPS** (Fig. 2g), which was taken as evidence of GSH-mediated loss of the bound Cu(II) cation. The Cu(II) complex used in this study (**CA9-BPS-Cu(II)**) was purified using HPLC after adding 1.0 equiv. of Cu(II) perchlorate to **CA9-BPS**. The integrity of **CA9-BPS-Cu(II)** prepared in this way was confirmed using HPLC and ESI-MS analyses (Supplementary Figs. 4 and 48).

Photodynamic and chemodynamic properties of CA9-BPS-Cu(II) and CA9-BPS. The ability of **CA9-BPS-Cu(II)** and **CA9-BPS** to produce $^1O_2$ under photo-irradiation was measured in acetonitrile solution using 1,3-diphenylisobenzofuran (DPBF) as a $^1O_2$ indicator[46]. Irradiation of **CA9-BPS-Cu(II)** and **CA9-BPS** solutions, respectively, in the presence of DPBF with a 660 nm laser irradiation decreased the spectral absorption intensity ascribed to DPBF, as would be expected under conditions of $^1O_2$ production (Figs. 3a, b). In contrast, no spectral changes were observed in the absence of photo-irradiation (Supplementary Fig. 5). In addition, negligible photothermal effects were seen for either **CA9-BPS-Cu(II)** or **CA9-BPS** in biomimetic model systems, including MDA-MB-231 cell cytosol extract (20 μg/mL), under conditions of high power density photo-irradiation (2.0 W/cm^2, 10 min; 1200 J/cm^2) (Supplementary Fig. 6). The rate of $^1O_2$ production for the **CA9-BPS-Cu(II)** solution was about 2.5 times smaller than that for **CA9-BPS** under these experimental conditions (Fig. 3d). Nevertheless, it was concluded that both systems are capable of acting as PDT photosensitizers.

Furthermore, treating **CA9-BPS-Cu(II)** with Na_2S, a copper precipitant, increased the rate of $^1O_2$ production to a similar level as that of **CA9-BPS** under identical conditions, which could be due to the release of the Cu(II) cation triggered by Na_2S, leading to regeneration of the more active metal-free form, **CA9-BPS** (Fig. 3c). On this basis we propose that the lower $^1O_2$ production efficacy of **CA9-BPS-Cu(II)** relative to **CA9-BPS** is due in large measure to quenching of the excited state by the Cu(II) center.

To probe whether **CA9-BPS-Cu(II)** would act to release Cu(I) under reducing conditions, a mixed solution containing **CA9-BPS-Cu(II)** and GSH was prepared. The addition of bathocuproinedisulfonic acid disodium salt (BCDS), a specific Cu(I) chelating agent[47], to this mixed solution revealed a new absorption band at 480 nm, which could be ascribed to the formation of the BCDS-Cu(I) complex (Figs. 3e, f). Furthermore, the addition of BCDS to **CA9-BPS-Cu(II)** solutions containing the endogenous reductants Cys and AA showed similar absorption bands at 480 nm (Supplementary Fig. 7). In contrast, this band at 480 nm was not observed when a solution of **CA9-BPS-Cu(II)** was tested in the absence of an endogenous reductant as a function of time (for 1 h to 24 h) (Supplementary Figs. 8a, c). Similar results were seen for **CA9-BPS-Cu(II)** when the same experiment was performed using an RPMI cell culture media containing a diversity of biological species, including amino acids, inorganic salts, and vitamins (10% FBS, without phenol red) (Supplementary Figs. 8b, d). This difference was consistent with the design expectation, namely that cellular reductant-mediated reduction of **CA9-BPS-Cu(II)** promotes the release of free Cu(I).

It has been shown that Cu(I)-catalyzed Fenton-like reactions can efficiently produce ·OH in the presence of H_2O_2 in weakly acidic tumor microenvironments[48]. To confirm that **CA9-BPS-Cu(II)** could promote a Cu(I)-catalyzed Fenton-like reaction, ·OH production by **CA9-BPS-Cu(II)** was measured using terephthalic acid (TPA), a known ·OH trap[49]. As shown in Figs. 3g, h, the addition of H_2O_2 to a mixed solution of **CA9-BPS-Cu(II)** and GSH led to a dramatic enhancement in the TPA emission band at 440 nm after 1 h of incubation. In contrast, a negligible change was observed in a mixed copper-free solution consisting of **CA9-BPS** and GSH under identical experimental conditions. This was also true for solutions containing TPA only or TPA + H_2O_2. Taken together, these findings suggest that **CA9-BPS-Cu(II)** could play a role as a Fenton reaction-assisted PDT sensitizer that is effective in tumor microenvironments.

***In vitro* characterization of CA9-BPS-Cu(II) as a putative anticancer sensitizer.** Prior to the *in vitro* characterization of **CA9-BPS-Cu(II)**, the cellular expression of CA9 in various breast cancer cells (MDA-MB-231, MCF-7, T47D, SK-BR-3, BT-474, ZR-75-1, Hs578T, and MDA-MB-453) and non-malignant breast epithelial cells (MCF10A) was confirmed by western blot analysis. As shown in Supplementary Fig. 9, the expression of CA9 was considerably higher in MDA-MB-231 cells than in other breast cancer cells, including MCF-7. Expression of CA9 was also observed in the MDA-MB-453 cells under the identical experimental conditions. This finding is in agreement with a previous report[50] and is considered supportive of the notion that CA9-targeting systems, such as **CA9-BPS-Cu(II)**, would display excellent CSC targeting affinity[41]. Therefore, high CA9 MDA-MB-231 breast cancer cells were used to assess the therapeutic potential of **CA9-BPS-Cu(II)**.

To validate the **CA9-BPS-Cu(II)** as a putative anticancer sensitizer, the intracellular ROS levels were measured in the MDA-MB-231 cell line using an intracellular ROS probe 2',7'-dichlorodihydrofluorescein diacetate (DCFH-DA)[51]. Upon subjecting MDA-MB-231 cells incubated with **CA9-BPS** and **CA9-BPS-Cu(II)** (5 μM, respectively) for 24 h to 660 nm photo-irradiation (100 mW/cm^2, 5 min; 30 J/cm^2), significant fluorescence enhancement of the DCFH-DA was observed for both **CA9-BPS-Cu(II)** and **CA9-BPS**. Importantly, however, the fluorescence intensity in the **CA9-BPS-Cu(II)**-treated group was about 1.4 times greater than that of the corresponding group treated with **CA9-BPS** (Fig. 4a).

Under identical photo-irradiation conditions, the **CA9-BPS-Cu(II)**-mediated production of $^1O_2$ in MDA-MB-231 cells was measured using singlet oxygen sensor green (SOSG)[52] as a $^1O_2$ probe. As shown in Supplementary Fig. S10, subjecting MDA-MB-231 cells incubated with **CA9-BPS-Cu(II)** to photo-irradiation with 660 nm light led to significant fluorescence enhancement, as would be expected for $^1O_2$ production under these conditions. A slightly weaker signal was observed for **CA9-BPS** under the same experimental conditions. In contrast, in the absence of photo-irradiation, very weak fluorescence intensities were observed for both **CA9-BPS-Cu(II)** and **CA9-BPS**.

Next, the **CA9-BPS**s-mediated production of ·OH in MDA-MB-231 cells was measured using hydroxyphenyl fluorescein (*HPF*), a commercial ·OH probe[53]. As shown in Fig. 4b, the addition of **CA9-BPS-Cu(II)** to MDA-MB-231 cells containing HPF increased the fluorescence of *HPF* slightly relative to that

of control. A fluorescence feature ascribable to HPF was observed for **CA9-BPS-Cu(II)**-treated cells in the presence of photo-irradiation. Of note is that under identical photo-irradiation conditions, about 1.2 times greater ·OH production was observed in the case of **CA9-BPS-Cu(II)**-treated cells than those treated with **CA9-BPS** (Fig. 4b). These results are interpreted in terms of both systems acting as Type I PDT agents thus giving rise to radicals, including ·OH production. The enhanced ·OH production in **CA9-BPS-Cu(II)** is rationalized in terms of a combined CDT/PDT effect that serves to enhance the baseline PDT cytotoxicity.

As shown in Fig. 4c, pretreatment of L-buthionine sulfoximine (L-BSO), an inhibitor of *r*-glutamylcysteine synthetase, which reduces the levels of GSH[54], dramatically enhanced the HPF fluorescence in the cells incubated with **CA9-BPS-Cu(II)**, greater than in the cells with **CA9-BPS**. These results could be ascribed to the critical role of GSH, which is an antioxidant recognized for its ability to neutralize intracellular ·OH[55,56]. As inferred from inductively coupled plasma-mass spectrometry (ICP-MS) analyses, the amount of copper uptake inside **CA9-BPS-Cu(II)**-treated MDA-MB-231 cells was higher than that in control, $CuCl_2$, and **CA9-BPS**-treated groups (Fig. 4d). In addition, a significant decrease in intracellular GSH levels was observed in the **CA9-BPS-Cu(II)**-treated cell group (Fig. 4e).

Based on the results in Figs. 2 and 3, we conclude that the addition of **CA9-BPS-Cu(II)** into cancer cells, followed by reaction with endogenous reductants could promote demetallation and release Cu(I). The generated Cu(I) then produces ·OH in the tumor microenvironment. **CA9-BPS-Cu(II)** is also expected to reduce the GSH levels *via* oxidation of GSH to GSSG. The corresponding reduction in GSH levels could also be expected to enhance the cytotoxic effects arising from ·OH generation by **CA9-BPS-Cu(II)**. To the extent that this occurs, it would provide a synergistic effect that could abet cell apoptosis by increasing the ROS levels within the cancer cell.

The intracellular localization of **CA9-BPS-Cu(II)** was studied using the commercially available organelle-targeting trackers Mito-, ER-, and Lyso-Tracker Green®. These studies revealed that the red fluorescence of MDA-MB-231 cells incubated with **CA9-BPS-Cu(II)** and ascribed to the conjugate is distributed throughout the cell compartment, rather than within specific cell organelles (Fig. 4f and Supplementary Fig. 11).

Western blot analyses were then carried out in an effort to probe ROS-mediated cell death mechanisms[57]. In the absence of light irradiation, MDA-MB-231 cells treated with **CA9-BPS** or **CA9-BPS-Cu(II)** did not show significant changes in apoptosis-related markers. On the other hand, after photo-irradiation, **CA9-BPS-Cu(II)**-treated MDA-MB-231 cells showed an enhanced expression of pro-apoptotic proteins (Bax, C.Cas 3; Cleaved caspase 3) and reduced expression of anti-apoptotic protein (Bcl-2) compared to what was seen in the case of the **CA9-BPS**-treated cells (Fig. 4g). These results provide support for the core suggestion that CDT/PDT processes mediated by **CA9-BPS-Cu(II)** are effective in promoting cancer cell death.

Cytotoxicity of CA9-BPS-Cu(II) and CA9-BPS. To compare the relative *in vitro* cytotoxicity of **CA9-BPS-Cu(II)** and **CA9-BPS**, a cell viability assay was conducted with MDA-MB-231 cells. As shown in Fig. 5a, the

viability of the MDA-MB-231 cells treated with 30 μM **CA9-BPS-Cu(II)** was reduced (~16%), whereas only slight reduction was observed in **CA9-BPS**-treated cells under identical experimental conditions. On the contrary, the toxicity effects of **CA9-BPS-Cu(II)** or **CA9-BPS** at a concentration of < 80 μM were negligible in normal human fibroblasts BJ cells (Supplementary Fig. 12). From these results, it is evident that **CA9-BPS-Cu(II)** stimulates a CDT effect in MDA-MB-231 cells but produces little damage to BJ cells at the test concentrations, and the minimal damage seen for the BJ cells is ascribed to the extremely low concentration of CA9, as well as the low H_2O_2 activity, characteristic of this normal cell line[12,58].

To assess the benefit of the putative combined CDT/PDT effect, MDA-MB-231 cells were tested with **CA9-BPS-Cu(II)** in the presence and absence of laser irradiation. Under conditions of photo-irradiation (660 nm, 100 mW/cm^2, 5 min; 30 J/cm^2), the cytotoxic effect of **CA9-BPS-Cu(II)** was found to increase in a dose-dependent fashion. At equal concentrations (30 μM) and otherwise identical conditions, **CA9-BPS-Cu(II)** reduced the cell viability more effectively than **CA9-BPS** (~61% vs ~26%) (Fig. 5a). This relative increase in efficacy seen for **CA9-BPS-Cu(II)** is thought to reflect the ancillary therapeutic benefit of Cu(I)-mediated production of ROS, a CDT effect that might be enhanced, in part, by copper-catalyzed GSH depletion. Support for this latter proposition came from the finding that when the cells were pretreated with *N*-ethylmaleimide (NEM)[59], a GSH inhibitor, enhanced photocytotoxicity was observed for **CA9-BPS-Cu(II)** at low concentrations (< 10 μM) (Supplementary Fig. 13). This finding is consistent with the elevated levels of oxidative stress expected for cancer cells subjected to GSH depletion.

Superior cell death was observed in **CA9-BPS-Cu(II)**-treated high CA9 MDA-MB-231 cells (~61%) compared to **CA9-BPS-Cu(II)**-treated CA9 low MCF-7 cells (~26%) upon light irradiation at 660 nm under identical experimental conditions (Figs. 5a, b). As shown in Supplementary Fig. 14, confocal fluorescence imaging with propidium iodide (PI) staining revealed significant fluorescence enhancement in the MDA-MB-231 cells after 660 nm laser irradiation. However, in the case of MCF-7 cells, very weak fluorescent signals were observed. These findings are consistent with the effective killing observed in the case of the MDA-MB-231 cells, but not the MCF-7 cells.

Moreover, when the MDA-MB-231 cells were pretreated with acetazolamide as a presumed antagonist and CA9 siRNA to affect CA9 gene knockout, respectively, the photocytotoxicity of **CA9-BPS-Cu(II)** was reduced dramatically (Figs. 5c, d and Supplementary Figs. 15, 16). This finding is consistent with the proposed CA9 specificity of **CA9-BPS-Cu(II)**, which, as per the molecular design, is thought to arise from the conjugated acetazolamide ligand. Based on these results, we considered that **CA9-BPS-Cu(II)** would be effective as a photo-mediated cancer treatment for tumors characterized by high levels of CA9.

Hypoxia stabilizes the HIF1-alpha mediated signaling cascade, which confers resistance of cancer cells to conventional therapies, by reprogramming cell metabolism, inhibiting cell death signaling, and maintaining cancer stemness[60,61]. CA9 expression is positively regulated by HIF1-alpha, thus CA9-targeted therapy constitutes a promising strategy for hypoxic tumor therapy[62]. In accord with such expectations, we found that our **CA9-BPS**s give rise to a considerable anti-cancer effect even in hypoxic MDA-MB-231 cells (Supplementary Fig. 17). Based on an appreciation that 1) the cytotoxicity of **CA9-**

BPSs is highly dependent on CA9 expression levels (cf. Figs. 5c, d) and 2) endogenous CA9 levels are increased under hypoxic conditions (cf. Supplementary Fig. 17)[63], we propose that the enhanced cellular uptake of our **CA9-BPS** systems in hypoxic MDA-MB-231 cells and an inhibition of the CA9 signaling cascade acts to mitigate to some extent the therapeutic resistance of hypoxic MDA-MB-231 cancer cells.

Acetazolamide is known as a non-specific CAI. Appreciating this and with a desire to probe the putative correlation between our systems and CAs, including CA12, we performed *in vitro* cytotoxicity studies using low CA12 T47D and high CA12 BT-474 breast cancer cells (Supplementary Fig. 18, 19). As shown in Supplementary Fig. 19a, the photo-induced cytotoxicity effects of **CA9-BPS-Cu(II)** or **CA9-BPS** were minimal in the case of the low CA12 T47D breast cancer cells (~20% vs. ~15% cell death for **CA9-BPS-Cu(II)** and **CA9-BPS**, respectively, at 30 μM). Slightly stronger photo-induced cytotoxicity effects were observed for the high CA12 BT-474 breast cancer cells (~30% vs. ~27% cell death for **CA9-BPS-Cu(II)** and **CA9-BPS**, respectively, at 30 μM) under the same experimental conditions (Supplementary Fig. 19b). However, in both cases the effect was weaker than seen for the high CA9 MDA-MB-231 breast cancer cells (~61% vs. ~26% cell death for **CA9-BPS-Cu(II)** and **CA9-BPS**, respectively, at 30 μM) (Fig. 5a). Therefore, we speculate that our systems might also have a slight effect on CA12. However, the effect on CA9 is clear. In this context, we note that several CA9 isoform-specific inhibitors have now been described and are in clinical trials[64]. This foundational progress could set the stage for the development of improved multimodal systems based on, e.g., CSC targeting.

CSC targeting by CA9-BPS-Cu(II). CSCs are characterized by high basal levels of GSH (as a presumed intracellular antioxidant), as is also commonly observed in normal undifferentiated stem cells. Presumably, this provides a survival benefit by reducing ROS-derived oxidative stress[65,66]. Recently, studies have provided support for the proposition that copper- and copper-dependent proteins are promising cancer targets because of their vital roles in cell proliferation, survival, and metastasis, as well as modulators of intracellular redox status[67-69]. Additionally, significantly elevated CA9 expression levels have been reported in breast cancer CSCs[41,70,71].

Along with CA9, CD133 is a phylogenetically conserved *cell* surface marker associated with CSCs. Therefore, in this study, CD133-positive MDA-MB-231 cells were sorted by magnetic-activated cell sorting (MACS). The cytotoxicity of **CA9-BPS-Cu(II)** in CD133-positive MDA-MB-231 cells was significantly increased as compared to CD133 negative cells (Fig. 6a). This higher cytotoxicity might be due to the enhanced expression of CA9 in CD133-positive MDA-MB-231 cells compared to CD133-negative cells (Supplementary Fig. 20). It has been proposed that tumor spheroid formation is a characteristic of CSCs[72]. Primary and secondary sphere-formation assays were conducted with CD133-positive MDA-MB-231 cells using **CA9-BPS** and **CA9-BPS-Cu(II)** to ascertain their effect on the tumor-initiating ability of CSCs as reflected in the formation of tumor spheroids. In fact, the total number of tumor spheroids found in both primary and subsequent secondary sphere-formation assays was reduced upon treatment with **CA9-BPS** or **CA9-BPS-Cu(II)**. Importantly, evidence for a synergistic CDT/PDT effect was found in the case the **CA9-BPS-Cu(II)** treatment group as compared to the corresponding **CA9-BPS** treatment group

(Figs. 6b, c). Moreover, 4',6-diamidino-2-phenylindole (DAPI) and propidium iodide (PI) staining for dead cells inside of tumor spheroids provided support for the notion that **CA9-BPS-Cu(II)** could effectively target tumor spheroids composed of CD133-positive CSCs, compared to the control and **CA9-BPS** groups (Fig. 6d).

Next, CD44-positive and CD24-negative cells (a common breast cancer stem cell marker) were obtained from MDA-MB-231 cells using MACS sorting method. Key expression markers were confirmed by immunocytochemistry (Supplementary Fig. 21). In order to examine the effect of **CA9-BPS-Cu(II)** on tumor evolution and emergence of CSC, an ALDH1 activity assay was performed, since it has been previously shown that CSC expresses high levels of ALDH1 during tumor progression (Supplementary Fig. 22)[73]. Treatment with **CA9-BPS-Cu(II)** in conjunction with photo-irradiation served to lower the activity of ALDH1 as compared to what was found for the **CA9-BPS** treated cells. We thus conclude that the CSC ability was reduced not only in CD133 but also in CD44-positive and CD24-negative cells. Accordingly, we suggest that the synergistic targeting of oxidative stress by **CA9-BPS-Cu(II)** might allow for an effective entry into CSC eradication-focused cancer therapy[67,74].

It was also found that photo-irradiation in the presence of **CA9-BPS-Cu(II)** decreased so-called stemness (octamer-binding transcription factor-4; Oct4 and homeobox protein; Nanog), which is one of the criteria for CSCs. The corresponding protein expression was observed by immunocytochemistry of the tumor spheroids (Figs. 6e, f). The ROS generated by **CA9-BPS-Cu(II)** under photo-irradiation conditions increased the cytotoxicity of CD133-positive CSCs, presumably due to increasing ROS stress and escaping stemness.

Gene and protein expression of Sox9 (SRY-Box Transcription Factor 9), required for the expression of CSCs in breast luminal progenitor[75] and Stat3 (signal transducer and activator of transcription 3, an important transcriptional factor for normal stem cells and CSCs)[76] was also decreased when CD133-positive CSCs were treated with **CA9-BPS-Cu(II)** under conditions of photo-irradiation (Figs. 6e, f). Therefore, we conclude that the combined effect of CDT and PDT embodied in **CA9-BPS-Cu(II)** could trigger apoptosis in cancer cells and modulate the stemness of CSCs.

***In vivo* xenograft tumor imaging and photocytotoxic effects.** To confirm the *in vivo* anti-tumor efficacy of **CA9-BPS-Cu(II)**, xenograft mice models having two tumors in both femoral regions were prepared by inoculating MDA-MB-231 cells. CA9 expression within the tumor was proved via immunohistochemical staining of cryo-sectioned tumor tissue (Supplementary Fig. 23). To assess tumor-targeting efficiency of **CA9-BPS**s, *in vivo* and *ex vivo* fluorescence of xenograft mice was monitored after tail-vein injections of **CA9-BPS**s. Bright fluorescence ascribable to **CA9-BPS-Cu(II)** was observed at both the tumor sites with greater intensities than that observed for other organs, including the heart, liver, spleen, lung, and kidney (Figs. 7a, b). After a total of three injections (tail-vein injections 1 time a week for 3 weeks) of **CA9-BPS**s and following photo-irradiation (2.0 W/cm^2, 10 min; 1200 J/cm^2), a significant reduction in the size of the tumor was observed in the **CA9-BPS-Cu(II)** treatment group relative to the control and **CA9-BPS** treatment groups (Fig. 7c, d). HPF imaging of excised tumors showed that the fluorescence intensity

ascribable to HPF in the tumor tissue taken from the **CA9-BPS-Cu(II)** treatment group was greater than what was seen for the corresponding tissues for the **CA9-BPS** treated mice (Supplementary Fig. 24). We thus speculate that chemodynamic process could occur upon administration of **CA9-BPS-Cu(II)** in tumors and that these effects might be enhanced by PDT-induced ROS production.

Within the tumor tissues, the classic blue fluorescence ascribed to DAPI was minimal in the case of the **CA9-BPS-Cu(II)** treatment group as compared to the PBS and **CA9-BPS** treatment groups (Fig. 7e). Such findings are consistent with apoptosis being increased in the case of the **CA9-BPS-Cu(II)** treatment group. Further, quantitative analyses of the tumor weights (Fig. 7f) revealed a superior tumor suppression efficacy of **CA9-BPS-Cu(II)**, without an obvious effect on the overall body weight (Fig. 7g). A beneficial effect was observed for non-irradiated **CA9-BPS-Cu(II)** and irradiated **CA9-BPS**, although to a lesser extent than with irradiated **CA9-BPS-Cu(II)** (Figs. 7c, d, f). Similar anti-tumor effects were seen for **CA9-BPS**s when the same photocytotoxic experiments were performed using xenograft mice models having MDA-MB-453 cell lines that express high levels of CA9 (Supplementary Fig. 25). In addition to the high CA9 MDA-MB-231 and MDA-MB-453 tumor-bearing xenograft mice studies, the utility of **CA9-BPS**s was also assessed *in vivo* using CA9 low T47D tumor-bearing xenograft mice. These analyses revealed that neither **CA9-BPS-Cu(II)** nor **CA9-BPS** provided a significant therapeutic effect (Supplementary Fig. 26). This finding thus provides support for the design predicate that **CA9-BPS** and **CA9-BPS-Cu(II)** possess a high affinity for CA9 and can be effective in treating tumors that express CA9.

Conclusions

We successfully prepared a new Cu(II)-BODIPY PS complex (**CA9-BPS-Cu(II)**) containing a CA9-targeting ligand, acetazolamide, and demonstrated its efficacy in promoting a synergistic CDT/PDT effect with CSC targeting to enhance cancer therapy *in vitro* and *in vivo*. Compared to the metal-free systems **CA9-BPS**, **CA9-BPS-Cu(II)** exhibited intensified cytotoxicity against MDA-MB-231 cells under 660 nm laser photo-irradiation, attributed to the Cu(I)-mediated production of ROS, a CDT effect enhanced by PDT-induced ROS production and, in part, by copper-catalyzed glutathione depletion. Additionally, as inferred from studies with CD133-positive and CD133-negative MDA-MB-231 cells obtained by MACS, the CA9-targeting conferred by the acetazolamide subunit confirmed its CSC targeting ability. Furthermore, the *in vivo* studies validated its efficacy against tumor growth. Overall, the findings suggest that a higher efficacy of the combination of PDT and CDT, coupled with targeted ROS production, than the individual components. We believe that **CA9-BPS-Cu(II)** may have a role to play in controlling tumor regrowth and cancer metastasis and could prove particularly effective in targeting and eradicating CSCs.

References

1. Han, J. et al. Cancer stem cell-targeted bio-imaging and chemotherapeutic perspective. *Chem. Soc. Rev.* **49**, 7856–7878 (2020).

2. Tirino, V. et al. Cancer stem cells in solid tumors: an overview and new approaches for their isolation and characterization. *FASEB J.* **27**, 13–24 (2013).
3. Lucky, S. S., Soo, K. C. & Zhang, Y. Nanoparticles in photodynamic therapy. *Chem. Rev.* **115**, 1990–2042 (2015).
4. Shafirstein, G. et al. Interstitial photodynamic therapy—A focused Review. *Cancers* **9**, 12 (2017).
5. Master, A., Livingston, M. & Sen Gupta, A. Photodynamic nanomedicine in the treatment of solid tumors: perspectives and challenges. *J. Control. Release* **168**, 88–102 (2013).
6. Barathan, M. et al. Hypericin-photodynamic therapy leads to interleukin-6 secretion by HepG2 cells and their apoptosis via recruitment of BH3 interacting-domain death agonist and caspases. *Cell Death Discovery* **4**, e697 (2013).
7. Zheng, Y. et al. Photodynamic-therapy activates immune response by disrupting immunity homeostasis of tumor cells, which generates vaccine for cancer therapy. *Int. J. Biol. Sci.* **12**, 120–132 (2016).
8. Ferrario, A. et al. Antiangiogenic treatment enhances photodynamic therapy responsiveness in a mouse mammary carcinoma. *Cancer Res.* **60**, 4066–4069 (2000).
9. Kao, S. H., Wu, K. J. & Lee, W. H. Hypoxia, epithelial–mesenchymal transition, and TET-mediated epigenetic changes. *J. Clin. Med.* **5**, 24 (2016).
10. Casas, A., Perotti, C., Di Venosa, G. & Batlle, A. *Mechanisms of resistance to photodynamic therapy: an update* (ed. Rapozzi, V. & Jori, G.) 29–63 (Springer, 2015).
11. Lan, M. et al. Photosensitizers for photodynamic therapy. *Adv. Healthc. Mater.* **8**, 1900132 (2019).
12. Jung, H. S. et al. Overcoming the limits of hypoxia in photodynamic therapy: a carbonic anhydrase IX-targeted approach. *J. Am. Chem. Soc.* **139**, 7595–7602 (2017).
13. Wang, D. et al. Self-assembled single-atom nanozyme for enhanced photodynamic therapy treatment of tumor. *Nat. Commun.* **11**, 357 (2020).
14. Won, M. et al. An ethacrynic acid-brominated BODIPY photosensitizer (EA-BPS) construct enhances the lethality of reactive oxygen species in hypoxic tumor-targeted photodynamic therapy. *Angew. Chem., Int. Ed.* **60**, 3196–3204 (2020).
15. Yang, G.B. et al. Smart nanoreactors for pH-responsive tumor homing, mitochondria-targeting, and enhanced photodynamic-immunotherapy of cancer. *Nano Lett.* **18**, 2475–2484 (2018).
16. Dos Santos, A. F., de Almeida, D. R. Q., Terra, L. F., Baptista, M. S. & Labriola, L. Photodynamic therapy in cancer treatment-an update review. *J. Cancer Metastasis Treat.* **5**, 25 (2019).
17. Hwang, E. & Jung, H. S. Metal–organic complex-based chemodynamic therapy agents for cancer therapy. *Chem. Commun.* **56**, 8332–8341 (2020).
18. Tang, Z., Liu, Y., He, M. & Bu, W. Chemodynamic therapy: tumour microenvironment-mediated fenton and fenton-like reactions. *Angew. Chem., Int. Ed.* **58**, 946–956 (2019).
19. Szatrowski, T. P. & Nathan, C. F. Production of large amounts of hydrogen peroxide by human tumor cells. *Cancer Res.* **51**, 794–798 (1991).

20. Ma, B. et al. Self-assembled copper–amino acid nanoparticles for in situ glutathione “and” H_2O_2 sequentially triggered chemodynamic therapy. *J. Am. Chem. Soc.* **141**, 849–857 (2019).
21. Ju, E. et al. Copper(II)–graphitic carbon nitride triggered synergy: improved ROS generation and reduced glutathione levels for enhanced photodynamic therapy. *Angew. Chem., Int. Ed.* **55**, 11467–11471 (2016).
22. Rae, T. D., Schmidt, P. J., Pufahl, R. A., Culotta, V. C. & O’halloran, T. V. Undetectable intracellular free copper: the requirement of a copper chaperone for superoxide dismutase. *Science* **284**, 805–808 (1999).
23. Jomova, K. & Valko, M. Advances in metal-induced oxidative stress and human disease. *Toxicology* **283**, 65–87 (2011).
24. Lin, L. S. et al. Simultaneous fenton-like ion delivery and glutathione depletion by MnO_2 -based nanoagent to enhance chemodynamic therapy. *Angew. Chem., Int. Ed.* **57**, 4902–4906 (2018).
25. Franco, R. & Cidlowski, J. A. Apoptosis and glutathione: beyond an antioxidant. *Cell Death Differ.* **16**, 1303–1314 (2009).
26. George, S., Abrahamse, H. Redox potential of antioxidants in cancer progression and prevention. *Antioxidants* **9**, 1156 (2020).
27. Jing, T., Li, T., Ruan, Z. & Yan, L. pH- and glutathione-stepwise-responsive polypeptide nanogel for smart and efficient drug delivery. *J. Mater. Sci.* **53**, 14933–14943 (2018).
28. Liu, C. et al. Biodegradable biomimic copper/manganese silicate nanospheres for chemodynamic/photodynamic synergistic therapy with simultaneous glutathione depletion and hypoxia relief. *ACS Nano* **13**, 4267–4277 (2019).
29. Shih, C.-Y., Wang, P.-T., Su, W.-C., Teng, H. & Huang, W.-L. Nanomedicine-based strategies assisting photodynamic therapy for hypoxic tumors: State-of-the-art approaches and emerging trends. *Biomedicines* **9**, 137 (2021).
30. Xu, J. et al. All-in-one theranostic nanomedicine with ultrabright second near-infrared emission for tumor-modulated bioimaging and chemodynamic/photodynamic therapy. ACS Nano 14, 9613–9625 (2020).
31. Liu, C. et al. An open source and reduce expenditure ROS generation strategy for chemodynamic/photodynamic synergistic therapy. *Nat. Commun.* **11**, 1735 (2020).
32. Liu, Y. et al. All-in-one theranostic nanoagent with enhanced reactive oxygen species generation and modulating tumor microenvironment ability for effective tumor eradication. *ACS Nano* **12**, 4886–4893 (2018).
33. Lei, Z., Zhang, X., Zheng, X., Liu, S. & Xie, Z. Porphyrin–ferrocene conjugates for photodynamic and chemodynamic therapy. *Org. Biomol. Chem.* **16**, 8613–8619 (2018).
34. Zhao, Z. et al. Reactive oxygen species–activatable liposomes regulating hypoxic tumor microenvironment for synergistic photo/chemodynamic therapies. *Adv. Funct. Mater.* **29**, 1905013 (2019).

35. Liu, C. Biodegradable biomimic copper/manganese silicate nanospheres for chemodynamic/photodynamic synergistic therapy with simultaneous glutathione depletion and hypoxia relief. *ACS Nano* **13**, 4267–4277 (2019).
36. Lou, Y. et al. Targeting tumor hypoxia: suppression of breast tumor growth and metastasis by novel carbonic anhydrase IX inhibitors. *Cancer Res.* **71**, 3364–3376 (2011).
37. Pacchiano, F. et al. Ureido-substituted benzenesulfonamides potently inhibit carbonic anhydrase IX and show antimetastatic activity in a model of breast cancer metastasis. *J. Med. Chem.* **54**, 1896–1902 (2011).
38. Lima, A. R. et al. GC-MS-based endometabolome analysis differentiates prostate cancer from normal prostate cells. *Metabolites* **8**, 23 (2018).
39. Cecchi, A. et al. Carbonic anhydrase inhibitors. design of fluorescent sulfonamides as probes of tumor-associated carbonic anhydrase IX that inhibit isozyme IX-mediated acidification of hypoxic tumors. *J. Med. Chem.* **48**, 4834–4841 (2005).
40. Mokhtari, R. B. et al. Combination of carbonic anhydrase inhibitor, acetazolamide, and sulforaphane, reduces the viability and growth of bronchial carcinoid cell lines. *BMC Cancer* **13**, 378 (2013).
41. Lock, F. E. et al. Targeting carbonic anhydrase IX depletes breast cancer stem cells within the hypoxic niche. *Oncogene* **32**, 5210–5219 (2013).
42. Kamkaew, A. et al. BODIPY dyes in photodynamic therapy. *Chem. Soc. Rev.* **42**, 77–88 (2013).
43. Banci, L. et al. Affinity gradients drive copper to cellular destinations. *Nature* **465**, 645–648 (2010).
44. Jung, H. S. et al. Coumarin-derived Cu^{2+}-selective fluorescence sensor: synthesis, mechanisms, and applications in living cells. *J. Am. Chem. Soc.* **131**, 2008–2012 (2009).
45. Thordarson, P. Determining association constants from titration experiments in supramolecular chemistry. *Chem. Soc. Rev.* **40**, 1305–1323 (2011).
46. Morone, M. et al. Enhancement of two-photon absorption cross-section and singlet-oxygen generation in porphyrins upon β-functionalization with donor–acceptor substituents. *Org. Lett.* **8**, 2719–2722 (2006).
47. Campos, C., Guzmán, R., López-Fernández, E. & Casado, A. Evaluation of the copper(II) reduction assay using bathocuproinedisulfonic acid disodium salt for the total antioxidant capacity assessment: the CUPRAC-BCS assay. *Anal. Biochem.* **392**, 37–44 (2009).
48. Sun, S. et al. Tumor microenvironment stimuli-responsive fluorescence imaging and synergistic cancer therapy by carbon-dot–Cu^{2+} Nanoassemblies. *Angew. Chem., Int. Ed.* **132**, 21227–21234 (2020).
49. Charbouillot, T. et al. Performance and selectivity of the terephthalic acid probe for ·OH as a function of temperature, pH and composition of atmospherically relevant aqueous media. *J. Photochem. Photobiol., A.* **222**, 70–76 (2011).
50. Li, Y. et al. Expression and activity of carbonic anhydrase IX is associated with metabolic dysfunction in MDA-MB-231 breast cancer cells. *Cancer Invest.* **27**, 613–623 (2009).

51. Jakubowski, W. & Bartosz, G. 2,7-Dichlorofluorescin oxidation and reactive oxygen species: what does it measure? *Cell Biol. Int.* **24**, 757–760 (2000).
52. Prasad, A., Sedlářová, M. & Pospíšil, P. Singlet oxygen imaging using fluorescent probe Singlet Oxygen Sensor Green in photosynthetic organisms. *Sci. Rep.* **8**, 13685 (2018).
53. Kohanski, M. A., Dwyer, D. J., Hayete, B., Lawrence, C. A. & Collins, J. J. A common mechanism of cellular death induced by bactericidal antibiotics. *Cell* **130**, 797–810 (2007).
54. Reliene, R. & Schiestl, R. H. Glutathione depletion by buthionine sulfoximine induces DNA deletions in mice. *Carcinogenesis* **27**, 240–244 (2006).
55. Angsubhakorn, S., Get-Ngern, P., Miyamoto, M., Bhamarapravati, N. A single dose-response effect of aflatoxin B1 on rapid liver cancer induction in two strains of rats. *Int. J. Cancer* **46**, 664–668 (1990).
56. Mezyk, S. P. Rate constant determination for the reaction of hydroxyl and glutathione thiyl radicals with glutathione in aqueous solution. *J. Phys. Chem.* **100**, 8861–8866 (1996).
57. Mahmood, T. & Yang, P.-C. Western blot: Technique, theory, and trouble shooting. *N. Am. J. Med. Sci.* **4**, 429–434 (2012).
58. Sunwoo, K. et al. Mitochondrial relocation of a common synthetic antibiotic: A non-genotoxic approach to cancer therapy. *Chem* **6**, 1408–1419 (2020).
59. Giustarini, D., Dalle-Donne, I., Milzani, A., Fanti, P. & Rossi, R. Analysis of GSH and GSSG after derivatization with *N*-ethylmaleimide. *Nat. Protoc.* **8**, 1660–1669 (2013).
60. Jing, X. et al. Role of hypoxia in cancer therapy by regulating the tumor microenvironment. *Mol. Cancer* **18**, 157 (2019).
61. Samanta, D., Gilkes, D. M., Chaturvedi, P., Xiang, L. & Semenza, G. L. Hypoxia-inducible factors are required for chemotherapy resistance of breast cancer stem cells. *PNAS* **111**, E5429–E5438 (2014).
62. McIntyre, A. et al. Carbonic anhydrase IX promotes tumor growth and necrosis in vivo and inhibition enhances anti-VEGF therapy. *Clin. Cancer Res.* **18**, 3100–3111 (2012).
63. Kim, J. H. et al. A small molecule strategy for targeting cancer stem cells in hypoxic microenvironments and preventing tumorigenesis. *J. Am. Chem. Soc.* **143**, 14115–14124 (2021).
64. Singh, S., Lomelino, C. L., Mboge, M. Y., Frost, S. C. & McKenna, R. Cancer drug development of carbonic anhydrase inhibitors beyond the active site. *Molecules* **23**, 1045 (2018).
65. Miran, T., Vogg, A. T. J., Drude, N., Mottaghy, F. M. & Morgenroth, A. Modulation of glutathione promotes apoptosis in triple-negative breast cancer cells. *FASEB J.* **32**, 2803–2813 (2018).
66. Jeong, E. M. et al. Real-time monitoring of glutathione in living cells reveals that high glutathione levels are required to maintain stem cell function. *Stem Cell Rep.* **10**, 600–614 (2018).
67. Karginova, O. et al. Inhibition of copper transport induces apoptosis in triple-negative breast cancer cells and suppresses tumor angiogenesis. *Mol. Cancer Ther.* **18**, 873–885 (2019).
68. Denoyer, D., Masaldan, S., La Fontaine, S. & Cater, M. A. Targeting copper in cancer therapy: 'copper that cancer'. *Metallomics* **7**, 1459–1476 (2015).

69. Shin, J., Eskandari, A. & Suntharalingam, K. Modulating the chemical and biological properties of cancer stem cell-potent copper(II)-nonsteroidal anti-inflammatory drug complexes. *Molecules* **24**, 1677 (2019).
70. Akrap, N. et al. Identification of distinct breast cancer stem cell populations based on single-cell analyses of functionally enriched stem and progenitor pools. *Stem Cell Rep.* **6**, 121–136 (2016).
71. Chen, Z. et al. Differential expression and function of CAIX and CAXII in breast cancer: a comparison between tumorgraft models and cells. *PLoS One* **13**, e0199476 (2018).
72. Ishiguro, T. et al. Tumor-derived spheroids: relevance to cancer stem cells and clinical applications. *Cancer Sci.* **108**, 283–289 (2017).
73. Lucia Martinez-Cruzado, L et al. Aldh1 expression and activity increase during tumor evolution in sarcoma cancer stem cell populations. *Sci. Rep.* **6**, 27878 (2016).
74. Guo, F. et al. Inhibitory effect on ovarian cancer ALDH+ stem-like cells by disulfiram and copper treatment through ALDH and ROS modulation. *Biomed. Pharmacother.* **118**, 109371 (2019).
75. Domenici, G. et al. A Sox2–Sox9 signalling axis maintains human breast luminal progenitor and breast cancer stem cells. *Oncogene* **38**, 3151–3169 (2019).
76. Galoczova, M., Coates, P. & Vojtesek, B. STAT3, stem cells, cancer stem cells and p63. *Cell. Mol. Biol. Lett.* **23**, 12 (2018).

Declarations

Acknowledgments

This work was supported by CRI project (2018R1A3B1052702, JSK) and the Basic Science Research Programs (2020R1F1A1073235, HSJ and 2018R1A2B6002275, JH and 2022R1C1C2007637, SK) from the National Research Foundation of Korea (NRF) funded by the Ministry of Education. The work in Austin was supported initially by the National Institutes of Health (CA68682, JLS). Further support was provided by the Robert A. Welch Foundation (F-0018, JLS). We also gratefully acknowledge support from Korea University, Hyupsung University and the University of Texas at Austin.

Author contributions

H.S.J., J.L.S., J.H. and J.S.K. conceived the methodology and supervised the project. H.S.J. and S.K. contributed to the project design and, along with S.A. and H.P. carried out the synthetic experimental work. J.H. and M.W. performed the biological experiments. All authors prepared and edited the manuscript.

Competing interests

The authors declare no competing interest.

Additional information

Supplementary Information is available for this paper at https://www.nature.com/nchem/

Reprints and permission information is available online at https://www.nature.com/reprints.

Reprints and permissions / Correspondence and requests for materials should be addressed to J.S.K. (e-mail: jongskim@korea.ac.kr) or J.L.S. (e-mail: sessler@cm.utexas.edu).

Figures

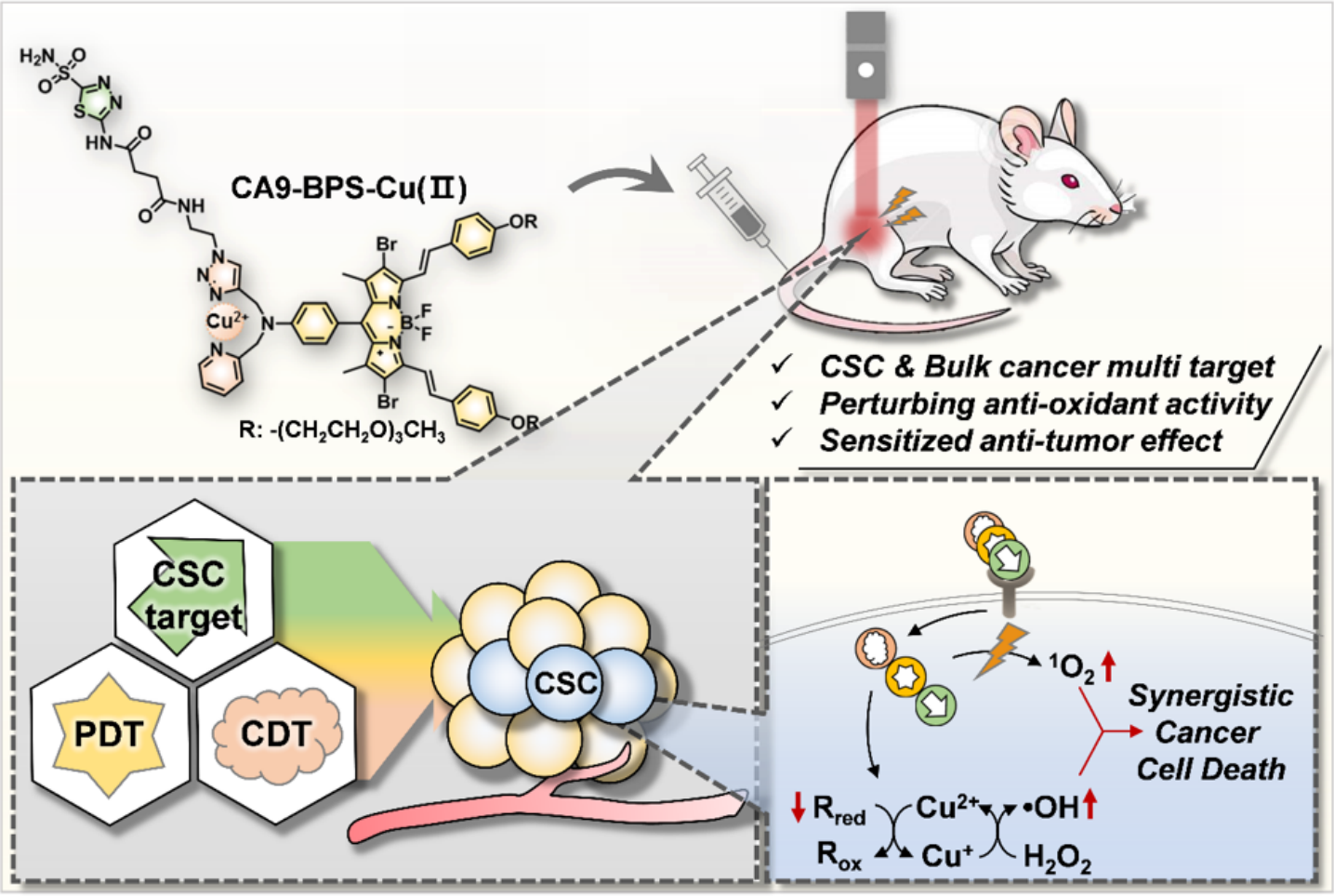

Figure 1

Schematic illustration of the synergistic anti-cancer effect expected to be produced by CA9-BPS-Cu(II). R_{red}, reduced form of endogenous reductants; R_{ox}, oxidized form of endogenous reductants.

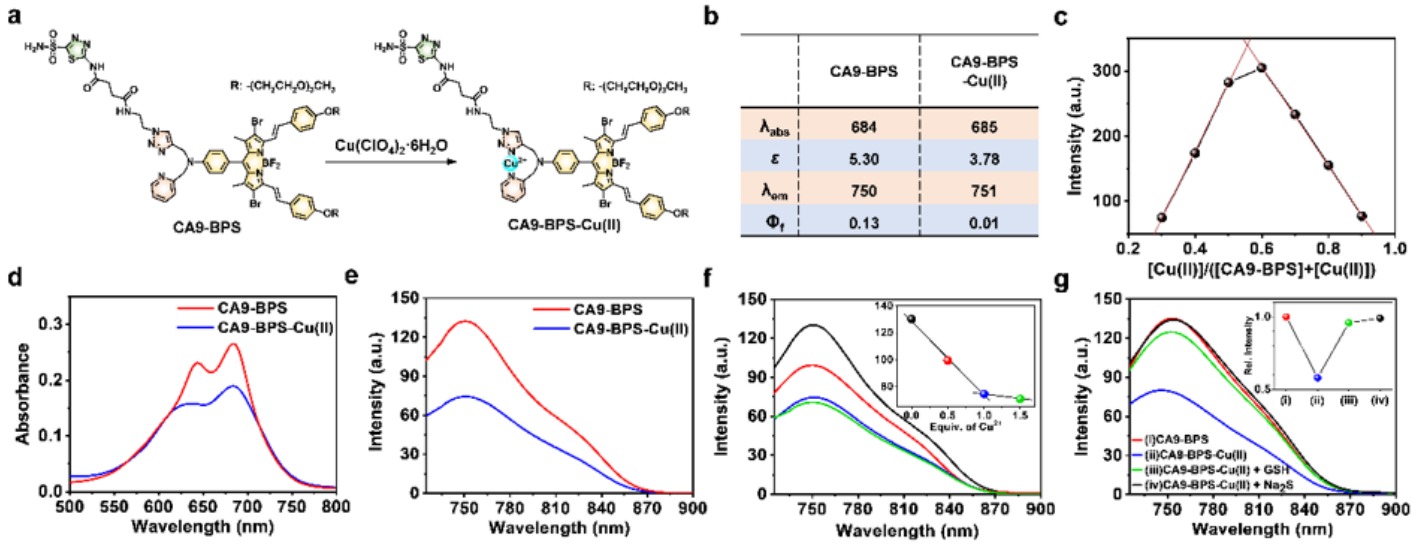

	CA9-BPS	CA9-BPS -Cu(II)
λ_{abs}	684	685
ε	5.30	3.78
λ_{em}	750	751
Φ_f	0.13	0.01

Figure 2

Effect of Cu(II) complexation on CA9-BPS. a Chemical structures of **CA9-BPS-Cu(II)** and **CA9-BPS**. **b** Photophysical properties of **CA9-BPS-Cu(II)** and **CA9-BPS** in PBS buffer solution (10 mM, pH 7.4, containing 5% DMSO). **c** Job's plot derived from the fluorescence changes seen for mixtures of **CA9-BPS** and **Cu(II)**. **d** Absorption and **e** fluorescence spectra of **CA9-BPS-Cu(II)** and **CA9-BPS** (both at 5.0 μM) in PBS buffer solution (10 mM, pH 7.4, containing 5% DMSO). **f** Fluorescence spectra of **CA9-BPS** (5.0 mM) in PBS buffer solution (10 mM, pH 7.4, containing 5% DMSO) recorded at various relative concentrations of Cu(II) (0 – 1.5 equiv.). Inset: Plot of emission intensity at 750 nm vs. Cu(II) equivalents. **g** Fluorescence spectra of **CA9-BPS** (red), **CA9-BPS-Cu(II)** (blue), **CA9-BPS-Cu(II)** treated with 30 μM GSH (green), and **CA9-BPS-Cu(II)** treated with 50 μM Na_2S (black) (5.0 μM in all cases) in PBS buffer solution (10 mM, pH 7.4, containing 5% DMSO). Excitation at 660 nm (slit = 20/20). The inset shows the relative change in intensity at 750 nm. λ_{abs}: absorption maximum wavelength (nm). ε: molar extinction coefficient ($\times 10^4$ M^{-1} cm^{-1}). λ_{em}: emission maximum wavelength (nm). Φ_f: fluorescence quantum yield.

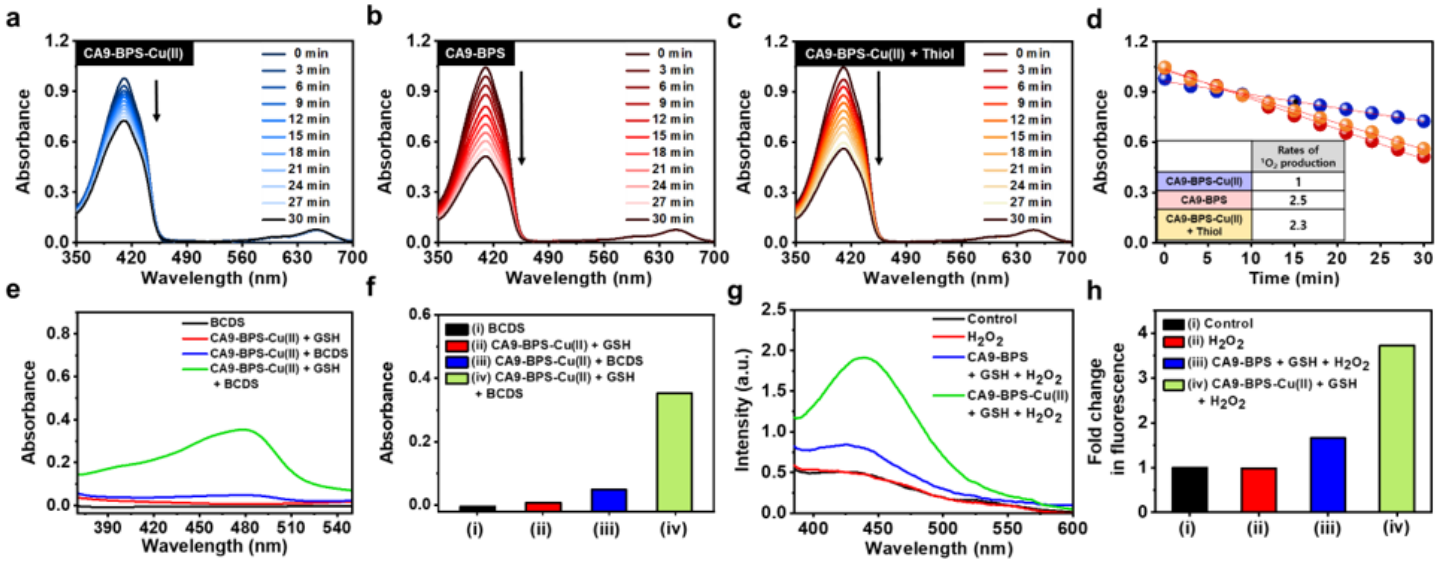

Figure 3

Photodynamic and chemodynamic properties of CA9-BPS-Cu(II) and CA9-BPS. a-d Photosensitized $^1O_2$ generation by **CA9-BPS-Cu(II)** and **CA9-BPS**. Time-dependent absorption spectral changes seen for 80 μM solutions of 1,3-diphenylisobenzofuran (DPBF) containing 1 μM of **a CA9-BPS-Cu(II)**, **b CA9-BPS** or **c CA9-BPS-Cu(II)** with added thiol mimic (1 equiv. Na_2S); irradiation was effected at 660 nm (slit width = 15-1.5, Xe-lamp) in all three experiments. **d** Plots of the change in the absorption intensity at 412 nm for the experiments shown in (**a**-**c**). **e**-**h** Chemodynamic properties of **CA9-BPS-Cu(II)**. **e** Absorption spectra of bathocuproinedisulfonic acid disodium salt (BCDS), upon treatment with **CA9-BPS-Cu(II)** in the presence and absence of GSH. **f** Histogram of the absorption intensity at 480 nm for the experiments shown in (**e**). **g** Emission spectra of terephthalic acid (TPA) upon treatment with **CA9-BPS-Cu(II)** or **CA9-BPS** in the presence of other species, including GSH, and H_2O_2. **h** Histogram of the emission intensity at 440 nm for the experiments shown in (**g**).

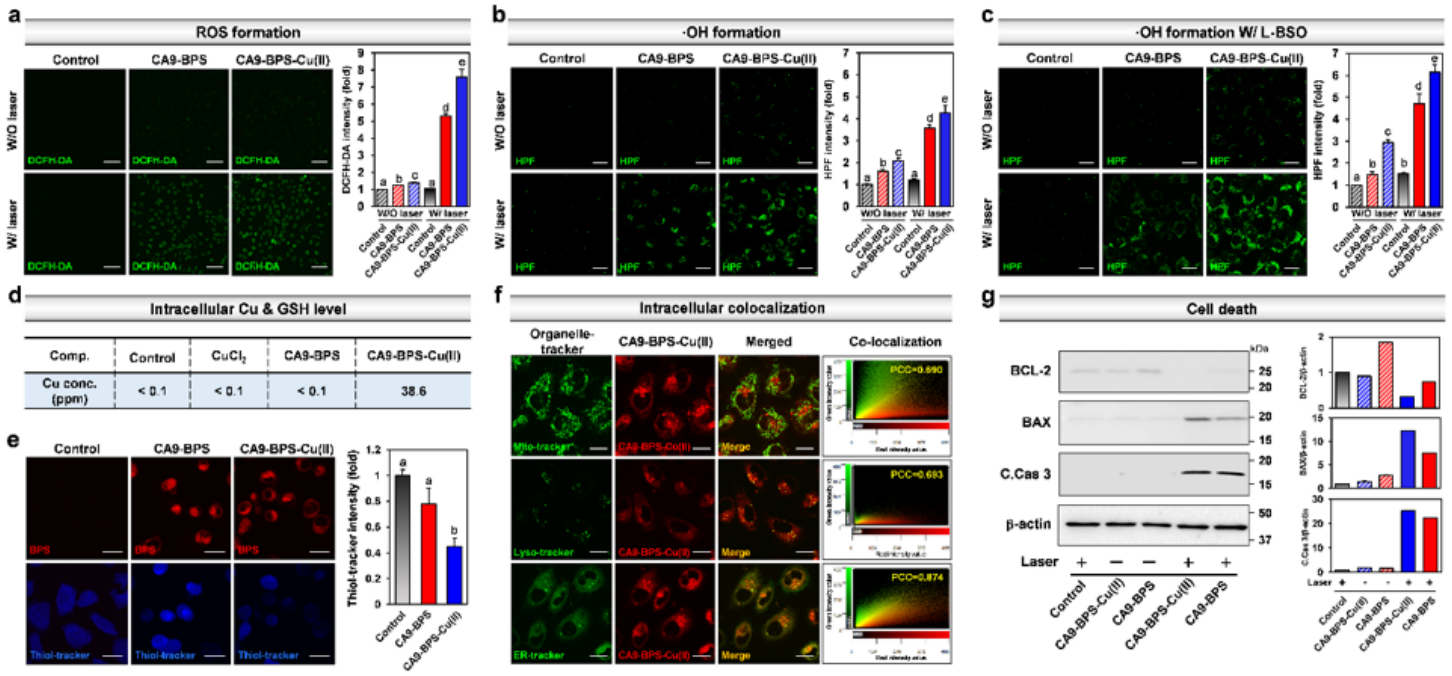

Figure 4

Mechanistic studies of CA9-BPS-Cu(II) and CA9-BPS. a Confocal fluorescence microscopic images of MDA-MB-231 cells incubated with the two **CA9-BPS**s considered in the present study (5 μM, respectively) and 2',7'-dichlorodihydrofluorescein diacetate (DCFH-DA; 10 μM) or **b-c** hydroxyphenyl fluorescein (*HPF;* 10 μM). The images were recorded with or without 660 nm laser irradiation (100 mW/cm^2, 5 min; 30 J/cm^2). For the experiment shown in (c), cells were subject to 100 μM L-buthionine sulfoximine (L-BSO) pretreatment 24 h before administering **CA9-BPS**s. Magnification & scale bars: (a) 20x &100 μm, (b,c) 90x & 20 μm. Histogram of the emission intensity was obtained by quantifying 5-region fields in cell images. **d** Intracellular copper accumulation: MDA-MB-231 cells were incubated with 20 μM of the indicated compounds for 24 h and washed with PBS and the copper concentrations in the cell lysates were measured using ICP-MS. **e** Confocal fluorescence microscopic images of MDA-MB-231 cells incubated with **CA9-BPS**s (5 μM) and with ThiolTracker®. Magnification: 120x. Scale bars: 20 μm. Histogram of the emission intensity of ThiolTracker® was obtained by quantifying 5-region fields in cell images. **f** Intracellular co-localization studies of **CA9-BPS-Cu(II)**: MDA-MB-231 cells were incubated with 5 μM of **CA9-BPS-Cu(II)** for 24 h. After being washed with PBS, Mito-, ER-, and Lyso-Trackers® (green) were added and the cells were incubated for an additional 30 min before the fluorescent images were recorded. Magnification: 142x. Scale bars: 20 μm. **g** Western blot analysis of cell death markers in **CA9-BPS-Cu(II)**- and **CA9-BPS**-treated MDA-MB-231 cells in the presence and absence of photo-irradiation (660 nm LED lamp, 100 mW/cm^2, 3 min; 18 J/cm^2). Data are presented as the mean, while the error bars indicate the standard deviation from the mean (n = 3). Statistical significance was determined by a two-way ANOVA test with a post-hoc Bonferroni test. Different letters signify datasets that are statistically distinct ($p < 0.05$).

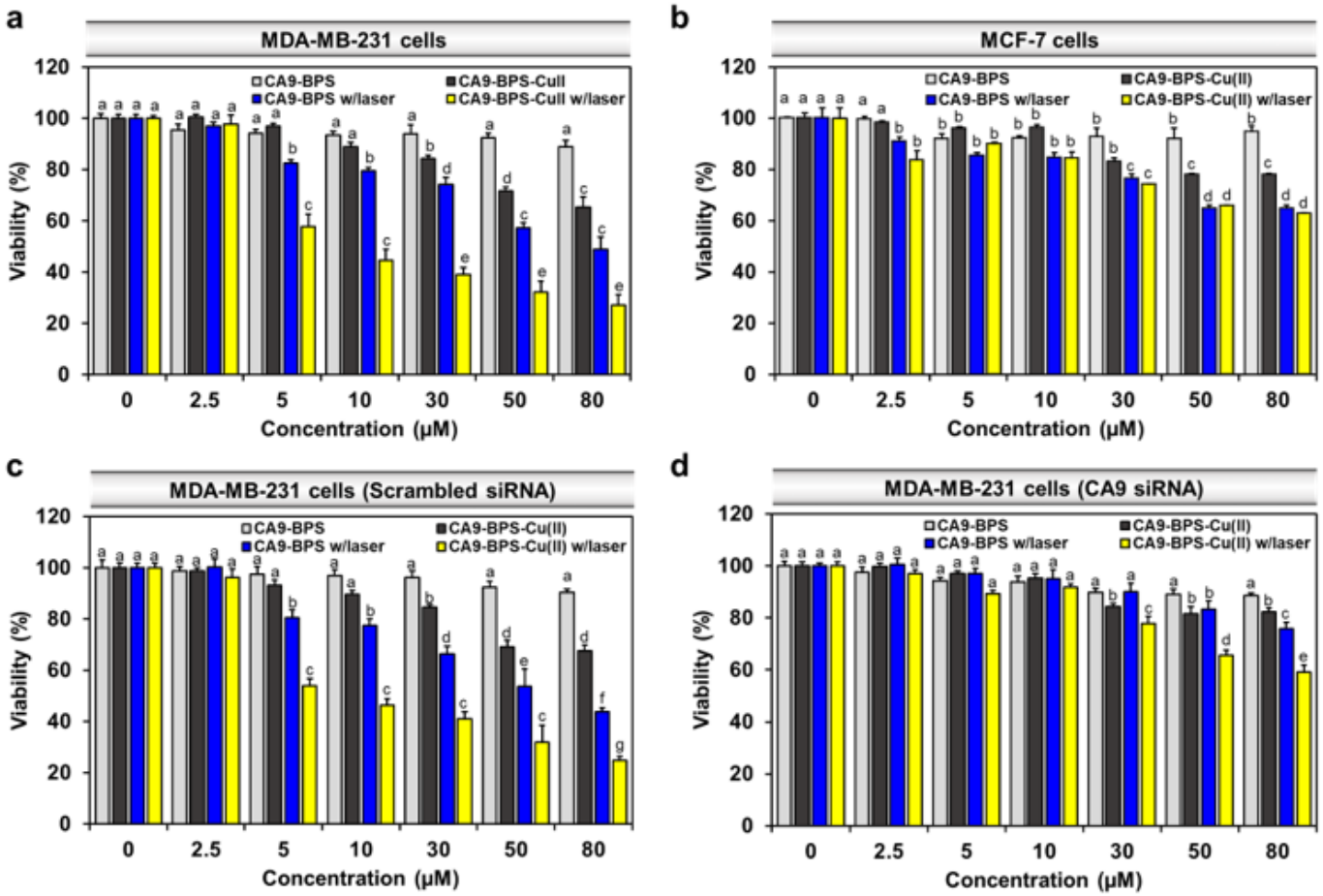

Figure 5

Cytotoxicity of CA9-BPS-Cu(II) and CA9-BPS. Cell viability of **a** MDA-MB-231 (CA9-highly expressed) and **b** MCF-7 (CA9-less significantly expressed) breast cancer cells treated with various concentrations (2.5 to 80 μM) of **CA9-BPS-Cu(II)** or **CA9-BPS** and 1% DMSO (as a control) for 12 h. The cells were photo-irradiated with a 660 nm LED lamp (100 mW/cm^2, 5 min; 30 J/cm^2). WST-8 assays were performed 12 h after irradiation. MDA-MB-231 (CA9-highly expressed) cells were transfected with **c** scrambled siRNA (siRNA control; 100 nM) and **d** CA9 siRNA (CA9 knockdown; 100 nM) for 4 h. Then, the cells were washed with PBS and further incubated for 24 h. The cells were treated with various concentrations (2.5 to 80 μM) of **CA9-BPS-Cu(II)** or **CA9-BPS** and 1% DMSO (as a control) for 12 h and were photo-irradiated with a 660 nm LED lamp (100 mW/cm^2, 5 min; 30 J/cm^2). WST-8 assays were performed 12 h after irradiation. Data are presented as the mean, while the error bars in **a**-**d** indicate the standard deviation from the means (n = 3). Statistical significance was determined using a two-way ANOVA test with a post-hoc Bonferroni test. Different letters signify statistically distinct data ($p < 0.05$).

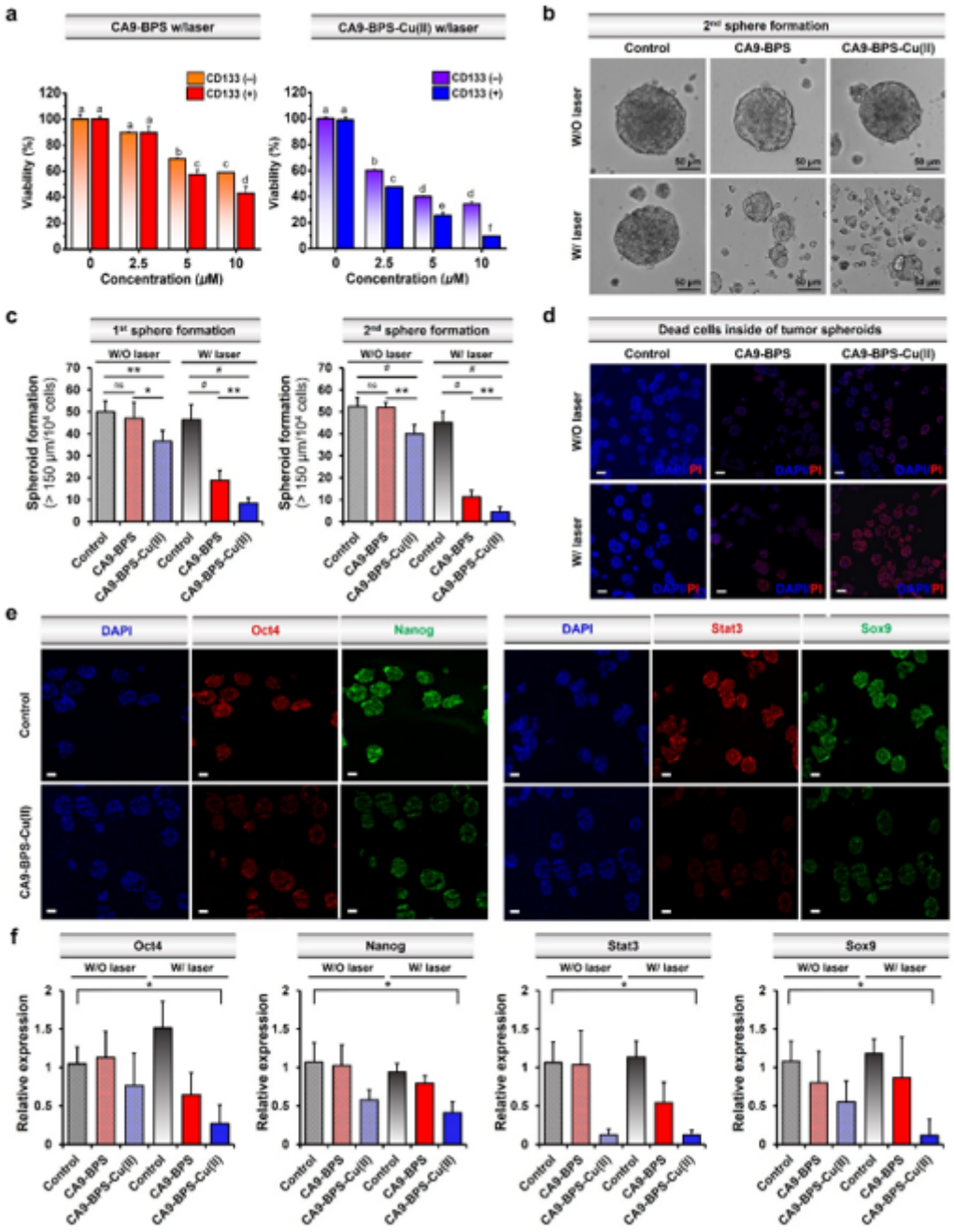

Figure 6

Therapeutic effects of CA9-BPS-Cu(II) and CA9-BPS on CSCs. a Cytotoxicity of **CA9-BPS-Cu(II)** and **CA9-BPS** toward CD133-positive and CD133-negative MDA-MB-231 cells obtained by magnetic-activated cell sorting (MACS). The sorted cells were seeded 1.0 × 10^4 per each well in a 96-well plate for WST-8 assay. **b** Images showing secondary tumor spheroid formation in MDA-MB-231 cells treated with **CA9-BPS-Cu(II)** or **CA9-BPS** (5 μM, respectively), or with 1% DMSO (as a control) with or without laser irradiation (660 nm; 100 mW/cm^2; 5 min; 30 J/cm^2) were recorded for 5 days. Magnification: 20x. Scale bars: 50 μm. **c** Total number of tumor spheroids found in both primary and subsequent secondary sphere-formation assays. **d** DAPI (blue) and PI (red) staining for dead cells inside of tumor spheroids formed by CD133-positive cells. **CA9-BPS-Cu(II)** or **CA9-BPS** (5 μM) was treated to tumor spheroids on the 2nd day and irradiated with a

660 nm lamp for 5 min on the 3rd day. Magnification: 10x. Scale bars: 100 μm. **e** Immunocytochemistry of tumor spheroids. The tumor spheroids were cultured and treated with 5 mM **CA9-BPS-Cu(II)** under the same conditions as in (d). Magnification: 10x. Scale bars: 100 μm **f** Gene expression of stemness-related genes by real-time PCR. Data are presented as the mean, while the error bars indicate the standard deviation from the mean (n = 3). Statistical significance was determined using the Student's t-test or one-way and two-way ANOVA test with a post-hoc Bonferroni test. Asterisks (*p<0.05, **p<0.01, #p<0.001) or different letters signify data that are statistically distinct (p < 0.05).

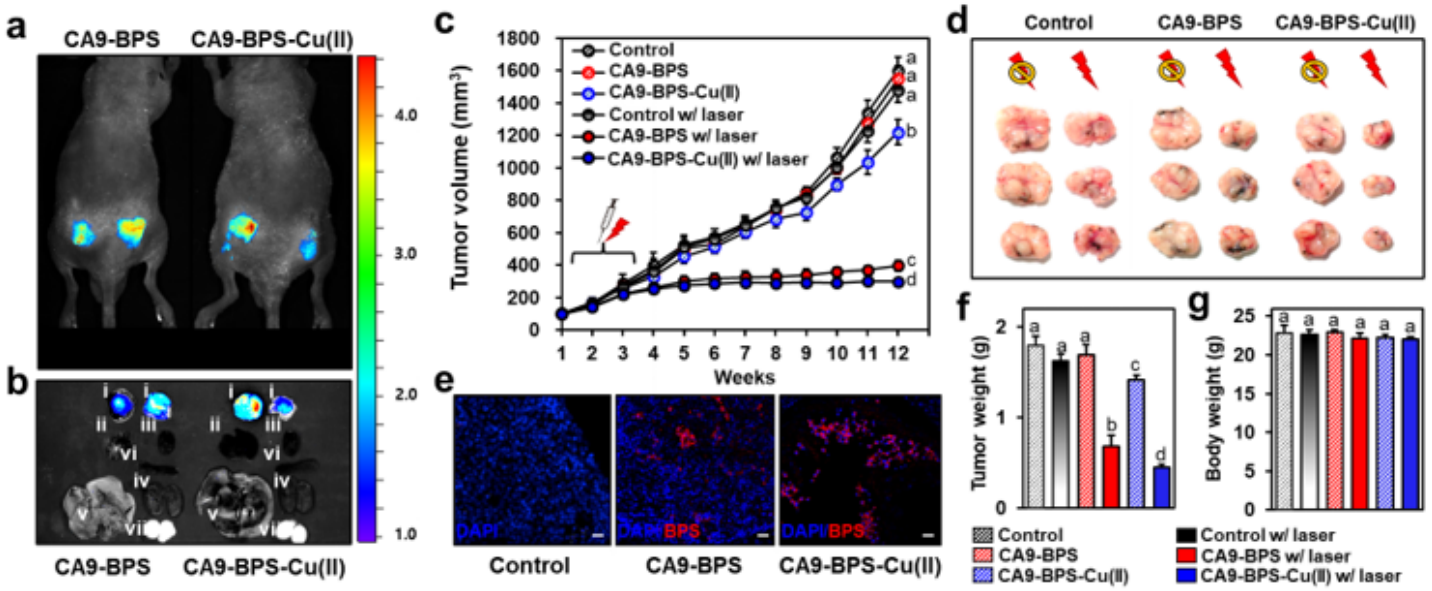

Figure 7

In vivo **diagnostic and photo-cytotoxic effects of CA9-BPSs. a** *In vivo* images of nude mice 4 h after tail-vein injection of **CA9-BPS**s. **b** Fluorescent *ex vivo* images of various organs (i: tumor, ii: lung, iii: heart, iv: spleen, v: liver, vi: kidney, vii: testis) taken from nude mice 6 h after tail vein injection of **CA9-BPS-Cu(II)** (right) or **CA9-BPS** (left). **c** Tumor volumes of the mice in the **CA9-BPS-Cu(II)** and **CA9-BPS** groups with or without PDT treatment. **d** Dissected tumors from each group. **e** Fluorescent images of 6 mm cryo-sectioned tumor tissue stained with DAPI (nuclei, blue) taken from each group after treatment. The red fluorescence is ascribed to the **CA9-BPS**s under study. Magnification: 100x. Scale bars: 30 μm. **f** Tumor weight and **g** body weight of the mice in the **CA9-BPS-Cu(II)** or **CA9-BPS** groups with or without PDT treatment. Data are presented as the mean, while the error bars indicate the standard deviation from the mean (n = 6). Statistical significance was determined using one-way and two-way ANOVA tests with associated post-hoc Bonferroni tests. Different letters signify data that are statistically distinct (p < 0.05).

Supplementary Files

This is a list of supplementary files associated with this preprint. Click to download.

- NCOMMS221757701FS.pdf
- ESINatCommresubmission220504.docx